ACCSCIENCE PUBLISHING

Materials Science in Additive Manufacturing

ORIGINAL RESEARCH ARTICLE

Impact behavior of AlSi10Mg porous structures with varying single-unit cell rotation angles fabricated via laser powder bed fusion

Xuezheng Yue[1], Hulin Tang[1], Songhao Lu[2], Rusheng Zhao[3], Boyoung Hur[4], Shiyue Guo[5]*, and Jincheng Wang[6,7]*

[1]Additive Manufacture International Lab, School of Materials Science and Engineering, University of Shanghai for Science and Technology, Shanghai, China

[2]Shanghai Micro Electronics Equipment (Group) Co., Ltd, Shanghai, China

[3]Department of Aerospace Engineering, Graduate School of Systems Design, Tokyo Metropolitan University, Tokyo 1910065, Japan.

[4]Department of Nano Advance Material, Gyeongsang National University, Jinju, South Gyeongsang, Korea

[5]Longzhong Lab, Wuhan University of Technology, Wuhan, Hubei, China

[6]Department of Mechanical Engineering, School of Engineering, The University of Western Australia, Perth, Western Australia, Australia

[7]Department of Mechanical Engineering, Faculty of Engineering and Information Technology, The University of Melbourne, Melbourne, Victoria, Australia

***Corresponding authors:**
Shiyue Guo
(guoshihiyue@lz-lab.com)
Jincheng Wang
(jincheng.wang@uwa.edu.au)

Citation: Yue X, Tang H, Lu S, *et al*. Impact behavior of AlSi10Mg porous structures with varying single-unit cell rotation angles fabricated via laser powder bed fusion. *Mater Sci Add Manuf*. 2025;4(2):025130019. doi: 10.36922/MSAM025130019

Received: March 29, 2025

Revised: April 18, 2025

Accepted: April 23, 2025

Abstract

Porous structures offer lightweight design and geometric flexibility for applications in transportation and bioengineering. Additive manufacturing, particularly laser powder bed fusion (LPBF), enables the fabrication of complex porous architectures. However, achieving an optimal balance between weight reduction and mechanical performance remains challenging. Therefore, further investigation into the design of porous structures is essential. This study explores the dynamic mechanical behavior of porous AlSi10Mg structures designed using a parametric modeling approach and the Voronoi tessellation algorithm. The structures, fabricated via LPBF, feature varying single-unit cell rotation angles and porosities. The dynamic mechanical behaviors were experimentally investigated under different impact energies to assess the influence of single-unit cell rotation on impact properties, complemented by finite element analysis simulations. The results indicate that a slight decrease in porosity by 10% (from 90% to 80%) significantly enhances energy absorption and impact resistance while maintaining lightweight features. Significant variations are observed in peak contact force and energy absorption trends. The results demonstrate that single-unit cell rotation improves impact resistance in certain cases, leading to significant enhancements in energy absorption, specific energy absorption, and specific strength, which increased by approximately 18.9% (P90), 17.1% (P90), and 79.5% (P80), respectively, for the dodecahedral (Dodeca)-C structure compared to the original Dodeca-A counterpart at impact of 124 J. In addition, Dodeca-C P80 showed a remarkable 73.1% increase in energy absorption compared to Dodeca-A P80 at a higher impact energy of 248 J. This study provides insights for optimizing porous structures while maintaining consistent unit cell configurations and identical porosity, with rotating unit cell angles enhancing impact resistance.

Keywords: Laser powder bed fusion; AlSi10Mg; Porous structures; Impact properties; Energy absorption; X-ray computed tomography

1. Introduction

Porous structures have recently attracted significant research interest due to their exceptional properties, including high specific strength,[1,2] excellent vibration and impact resistance,[3,4] low elastic modulus,[5] low thermal conductivity,[6] and superior specific energy absorption (SEA).[7-9] These characteristics make them highly suitable for applications in aerospace, biomedical engineering, and other fields where effective energy absorption is crucial to minimize damage to internal components and personnel during impact events. In recent years, various energy absorption structures have been studied,[10-13] including column structures,[14] sandwich structures,[15] honeycomb structures,[16] foam structures,[17] triply periodic minimal surface structures,[8,18] and other lattice structures.[19,20] While these designs exhibit enhanced energy absorption capabilities, further optimization is still needed to maximize performance. For example, Serban *et al.*[21] demonstrated that controlling the relative density of porous structures can be achieved by adjusting key design parameters such as strut thickness, strut length, and fillet radius. Wu *et al.*[4] incorporated solid cylinders of varying diameters into lattice structures while maintaining similar porosity, significantly improving compressive strength and impact energy absorption. Adjusting these parameters makes it possible to achieve a balance that satisfies both the demand for lightweight characteristics and the requirements for strength. These findings underscore the potential of parameter tuning to optimize the trade-off between lightweight design and mechanical performance.

Given the importance of dynamic loading in practical applications, researchers are increasingly focusing on the dynamic characteristics of porous structures. Numerous studies[22-25] have investigated the dynamic mechanical properties of porous metal materials. For instance, Cao *et al.*[26] performed numerical simulations and theoretical analyses to systematically explore the dynamic mechanical properties of modified rhombic dodecahedron porous structures, suggesting that optimizing parameters can enhance their dynamic performance. It has also been reported that the dynamic fatigue strength of topologically optimized porous structures significantly exceeds that of rhombic dodecahedron structures composed of the same metal and exhibiting identical porosity levels.[2] Furthermore, Kim *et al.*[27] utilized a multiscale approach to evaluate the impact resistance of porous aluminum foam-filled components, demonstrating that these porous materials outperform hollow tube structures of equivalent weight in terms of energy absorption. While dodecahedral (Dodeca) and octahedral (Octa) structures are prevalent in porous materials and have attracted attention, existing research has predominantly concentrated on static deformations under various conditions, thus creating a gap in experimental evidence regarding their dynamic impact behavior.

Metal additive manufacturing (AM) technology, which allows precise control of geometric structures through layer-by-layer stacking, offers a promising solution for producing complex and functional solid and porous structures.[28,29] This technology has emerged as a supplementary technique to conventional manufacturing methods for producing metallic components,[30-32] while also achieving considerable mechanical performance for metals.[33-35] Laser powder bed fusion (LPBF), also known as selective laser melting, is a pivotal aspect of laser AM and serves as a versatile method for fabricating various metallic components with tuned microstructures for enhanced mechanical performance.[36] In addition, it facilitates surface treatments for improved corrosion resistance[37] and enables the exploration of flexible powder design.[38] Due to their lightweight nature, corrosion resistance, and other favorable properties, aluminum alloys are widely used in metal component manufacturing.[39-41] Among these, the AlSi10Mg alloy is particularly favored in LPBF technology due to its well-established melting characteristics and consistent mechanical properties within an optimized processing window.[42] As such, investigating the dynamic impact behavior of AlSi10Mg-based porous structures will provide insights into their mechanical response and energy absorption characteristics, focusing on the influence of unit cell design.

Recent literature[43] has highlighted differences in the load-carrying capacity of various bearing surfaces within a single-unit cell, providing a foundation for investigating the mechanical properties of rotating single-unit cell structures. Alterations in the angle of rotation influence these mechanical properties, as evidenced by findings[44] that demonstrate a notable correlation between compressive stress and the maximum angle of rotation, indicating a strong interaction. Several researchers[45] have explored the effects of rotation angle on the mechanical properties of helical structures using a bionic design approach, revealing variations in SEA in response to changes in rotation angle. However, there has been limited research on the influence of rotation angle on the mechanical behavior of lattice structures under dynamic loading conditions. Therefore, it is imperative to conduct a comprehensive investigation into how the rotation angle affects the mechanical properties and energy absorption of lattice porous structures in dynamic scenarios. This study further advances existing research on the dynamics of porous lattice structures by providing new insights into the effects of unit cell orientation and porosity level on impact resistance and energy absorption.

In this study, Dodeca and Octa porous structures with varying rotation angles were designed and fabricated using AlSi10Mg through LPBF technology. Scanning electron microscopy (SEM) and X-ray computed tomography (X-CT) were utilized to characterize the effects of LPBF process parameters on microstructure, defects, and dimensional resolution. The research focuses on the experimental investigation of the mechanical behavior of these porous metallic structures under dynamic loading conditions, supplemented by finite element analysis simulations. The deformation mechanisms were systematically examined, and the energy absorption properties of the structures were evaluated, emphasizing the significant influence of single-unit cell rotation on their performance. The ultimate aim is to provide theoretical insights to enhance the optimization and practical application of porous structures in engineering.

2. Materials and methods

2.1. Materials and manufacturing

This study used AlSi10Mg powder, supplied by Falcontech (China), to fabricate porous structures. As shown in Figure 1A, the powder has a spherical morphology with a particle size distribution of 10 – 55 µm and an average particle size of approximately 25 µm (Figure 1B). The detailed chemical composition is provided in Table 1.

The LPBF equipment used is the EOSINT M280, manufactured by EOS GmbH, Germany. The laser operates at a power of 370 W, with a controlled scanning speed of 1,335 mm/s. A powder layer thickness of 30 µm is maintained, with a rotating hatch angle of 67°, whereas the laser spot diameter is set at 170 µm. During fabrication, high-purity argon gas is introduced into the chamber to minimize oxidation (oxygen levels below 1,000 ppm) and ensure a stable processing environment.

2.2. Design of porous structures

The implementation of an organized Voronoi structure design method utilizing Rhinoceros 5 (McNeel, United States), along with its Grasshopper plugin (version 0.9.0076), was employed to create Dodeca and Octa structures. In Figure 2A, Dodeca-A P80 and Dodeca-A P90 designations correspond to 80% and 90% porosity levels, respectively. The cell geometry of Dodeca-B P80 and Dodeca-B P90 is achieved by rotating the single-unit cell 90° around the X-axis based on the position of Dodeca-A. In contrast, the geometry of Dodeca-C P80 and Dodeca-C P90 is formed by a 90° rotation around the Y-axis (Figure 2A). As shown in Figure 2B, the Octa-B P80 and Octa-B P90 structures are created by first rotating the Y-axis by 54.7° and then rotating the Z-axis by 45° of the single-unit cell relative to the position of Octa-A. These specific rotations are designed to optimize and compare mechanical performance and energy absorption by altering the alignment of the unit cells. The overall dimensions of all the samples are 30 × 30 × 30 mm^3. To maintain the load-carrying capacity of the structural rods, the Dodeca and Octa structures were designed to keep the rod diameters constant, whereas porosity was adjusted by varying the number of single cells.

2.3. Experimental and characterization methods

The impact resistance of various porous structures was evaluated using room temperature hammer impact testing with a hammer impact tester (CEAS9350, INSTRON, United States), as depicted in Figure 3. Three different test configurations were employed, and the experimental conditions are detailed in Table 2 for the investigation and

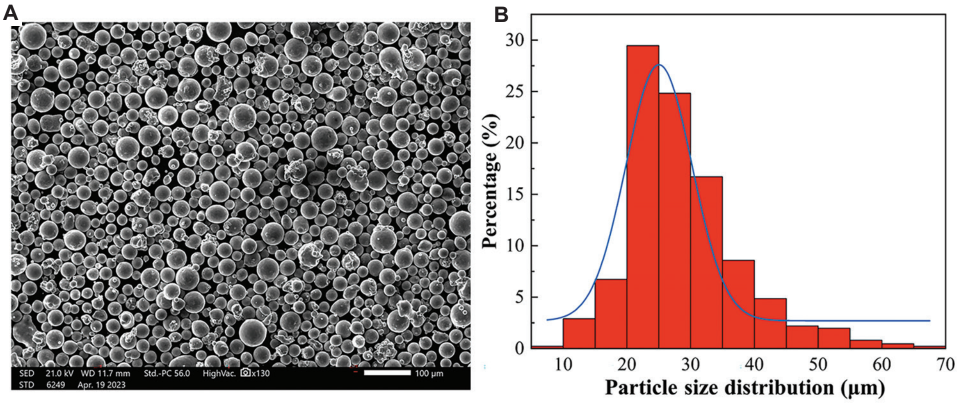

Figure 1. Powder characteristics. (A) Scanning electron micrograph shows the morphological characteristics of AlSi10Mg powder. Scale bar: 100 µm, magnification: 130×. (B) Particle size distribution of AlSi10Mg powder

Table 1. Chemical composition of AlSi10Mg powder

Element	Aluminium	Silicon	Magnesium	Iron	Copper	Manganese	Titanium	Oxygen
Composition (weight %)	Bal	10.20	0.35	0.038	<0.01	<0.01	<0.01	0.045

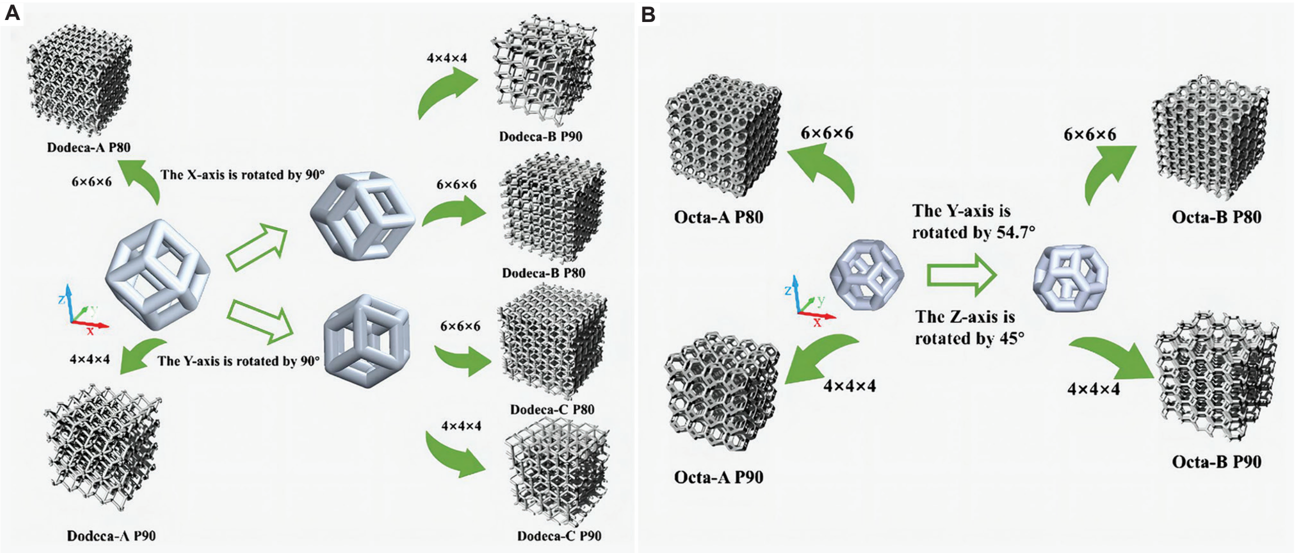

Figure 2. Design process of porous structures. (A) Dodeca structures, with Dodeca-A P80 and Dodeca-A P90 representing 80% and 90% porosity levels, respectively. Dodeca-B P80 and Dodeca-B P90 are achieved by a 90° rotation around the X-axis, whereas Dodeca-C P80 and Dodeca-C P90 are formed by a 90° rotation around the Y-axis. (B) Octa structures, where Octa-B P80 and Octa-B P90 are created by rotating the Y-axis by 54.7° and the Z-axis by 45° from the position of Octa-A

Abbreviations: Dodeca: Dodecahedral; Octa: Octahedral

comparison of low, medium, and high-impact energies. Three samples were tested under each condition to ensure the reliability and repeatability of the presented results. The microstructure of the samples was prepared through grinding and polishing for SEM analysis of the LPBF-fabricated AlSi10Mg samples. The X-CT (GE Vtomex system, General Electric Company, USA) analysis was performed using a scanning voltage of 130 kV, a current of 150 µA, and a spatial resolution of 5.5 µm. Cross-sectional CT images were obtained to evaluate the internal structure and morphology of the samples.

2.4. Numerical analysis of impact behavior

The impact process, characterized by its instantaneous nature and inherent difficulty in direct observation, is more effectively examined through finite element analysis simulations. The geometric model was imported into the ANSYS/LS-DYNA software (version ANSYS 2023 R1) (Ansys Inc., United States) for numerical analysis. Notably, considering various factors such as accuracy and cost-effectiveness, a tetrahedral mesh type was selected, with a final mesh size of 0.25 mm determined through mesh sensitivity tests conducted on the finite element model's mesh size and density.

The fracture criterion for AlSi10Mg porous structures can be described using the Johnson–Cook fracture criterion, expressed in Equations I and II:[46-48]

$$\varepsilon_0 = \left[D_1 + D_2 exp(D_3\sigma^*)\right]\left(1 + D_4 \ln \dot{\varepsilon}_p^*\right)\left(1 + D_5 T^*\right) \quad \text{(I)}$$

$$\sigma^* = \sigma_m / \sigma_{Mises} \quad \text{(II)}$$

where ε_0 represents the fracture strain, σ^* denotes stress triaxiality, σ_m stands for hydrostatic stress, σ_{Mises} represents Mises equivalent stress, and $D_1 - D_5$ encompass the material model parameters, $\dot{\varepsilon}^*$ is the dimensionless plastic strain rate. Relevant parameters, including density, elastic modulus, and Poisson's ratio, are shown in Table 3.

2.5. Energy absorption properties and evaluation indicators

Three main energy absorption metrics were utilized to effectively evaluate the dynamic energy absorption performance of porous structures: Peak force, energy absorption (E_a), and SEA. In addition, the specific strength (S_p) index serves as a crucial performance indicator. Peak force represents the maximum initial force exerted during the entire energy absorption process. These performance indicators provide valuable information regarding a structure's capacity to dissipate impact energy and can be utilized to compare the performance of different porous structures.

E_a is obtained by integrating the force-displacement curve under impact and is expressed as Equation III:[49]

$$E_a = \int_0^d F(x)\,d(x) \tag{III}$$

where F is the force and $d(x)$ is the displacement.

SEA is a normalized measure of the energy absorbed per unit mass of the porous structures. It is calculated by dividing the E_a by the mass of the sample,[49] as shown in Equation IV:

$$SEA = \frac{E_a}{m} \tag{IV}$$

where m is the mass of the sample.

S_p is considered to be an important parameter to characterize the properties of a material and is expressed as Equation V:

$$S_p = \frac{S_t}{\rho'} \tag{V}$$

where S_p is the specific strength (i.e., strength-to-weight ratio), S_t is the stress of the sample, and ρ' is the relative density of the sample.

Table 2. Falling hammer impact test parameters for the laser powder bed fusion-built porous structures

Method	Quality of the hammer (kg)	Impact energy (J)	Impact velocity (m/s)
M1	14.858	41	2.340
M2	14.858	124	4.090
M3	14.858	248	5.800

3. Results and discussion

3.1. Microstructure

As shown in Figure 4, the actual AlSi10Mg porous structures

Table 3. Parameters of the Johnson–Cook fracture criterion for laser powder bed fusion-built AlSi10Mg

Parameters	D1	D2	D3	D4	D5	ρ (kg/m^3)	E (Gpa)	v
Value	0.04704	1.155	−0.841	−0.042	0	2680	38	0.3

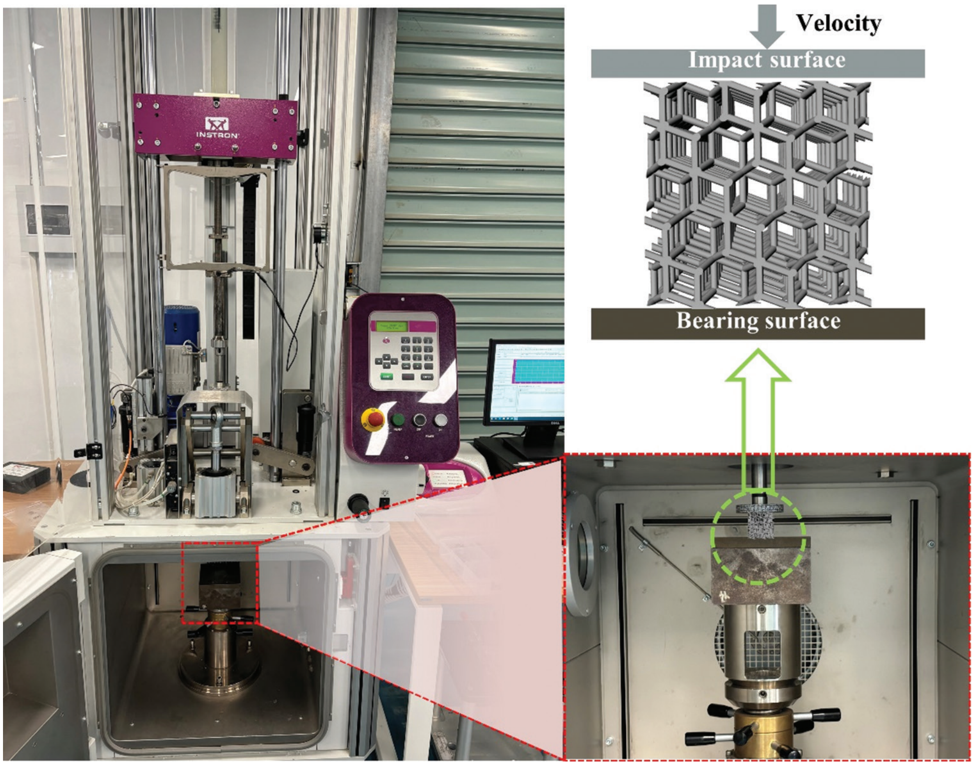

Figure 3. Diagram illustrates the falling hammer impact test equipment setup, including the hammer, impact specimen, and schematic representation of the test direction

were fabricated using LPBF according to the design models. The Dodeca and Octa structures are presented with designed 80% and 90% porosities labeled as P80 and P90, respectively. Specifically, Figure 4A and B illustrate the Dodeca-A, Dodeca-B, and Dodeca-C structures with 80% and 90% porosity, whereas Figure 4C and D display the Octa-A and Octa-B structures with the designed porosity levels, accordingly. It can be observed that the LPBF-built AlSi10Mg structures exhibit a high dimensional resolution finish under the optimized process parameters, which aligns with the high precision of the LPBF process.[42] Three identical structures were produced and tested in repeated experiments to ensure repeatability. However, slight deviations from macro to micro levels between the theoretical design dimensions and the actual manufactured samples can occur due to residual powder adhesion and localized over-melting in certain overhang regions during the LPBF process.[33] Therefore, further characterization of the micro-level differences is needed to assess the effects of LPBF manufacturing parameters on dimensional accuracy and to minimize the impact of these differences on the evaluation of dynamic performance.

Figure 5A and B present a comparison of the X-CT reconstructed models of the Octa-A structures fabricated from LPBF-built AlSi10Mg alloy, featuring porosities of 80% and 90% (i.e., Octa-A P80 and Octa-A P90), with their corresponding theoretical design models. The comparison reveals that the dimensional disparity between the reconstructed models and the theoretical designs falls within a narrow range of 1.3% – 3.45% (Figure 5C), further confirming high accuracy in the LPBF manufacturing process. Furthermore, Figure 5C and D provide a comparative analysis of the theoretical and actual volumes of the structures, demonstrating that the deviation in volume remains within 4%. This minimal deviation indicates a good consistency between the reconstructed models and the theoretical designs, suggesting that the manufacturing process effectively replicates the intended geometries. As a result, the impact of manufacturing variations on the mechanical properties of the LPBF-built Dodeca and Octa AlSi10Mg structures is considered negligible in this study. This consistency provides a solid foundation for analyzing the impact behavior of different porous structures, enabling accurate assessments of their performance under dynamic loading conditions.

Figure 6A presents SEM images of the sample surface, revealing a significant number of particles adhered to the porous structure. These observations are consistent with findings reported by Al-Ketan *et al.*[50] In addition, Figure 6B illustrates the melt pool tracks and morphologies, revealing very few irregular pore defects in the LPBF-fabricated AlSi10Mg samples. Measurement results indicate that the densification rate of the sample is 99.4% (i.e., high relative density). The schematic laser scanning path during the melting process is illustrated in Figure 6C, with an angle increment of 67° for each layer, which aligns with Figure 6B.

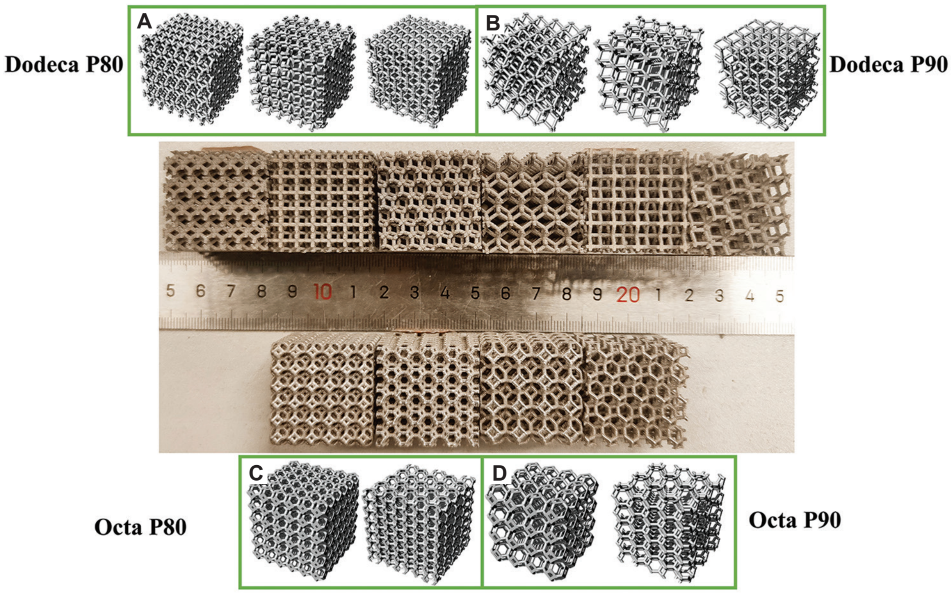

Figure 4. Dodeca and Octa AlSi10Mg structures with 80% and 90% porosity were prepared through laser powder bed fusion according to the designed models. (A) Dodeca-A, Dodeca-B, and Dodeca-C with 80% porosity, (B) Dodeca-A, Dodeca-B, and Dodeca-C with 90% porosity, (C) Octa-A and Octa-B with 80% porosity, and (D) Octa-A and Octa-B with 90% porosity
Abbreviations: Dodeca: Dodecahedral; Octa: Octahedral

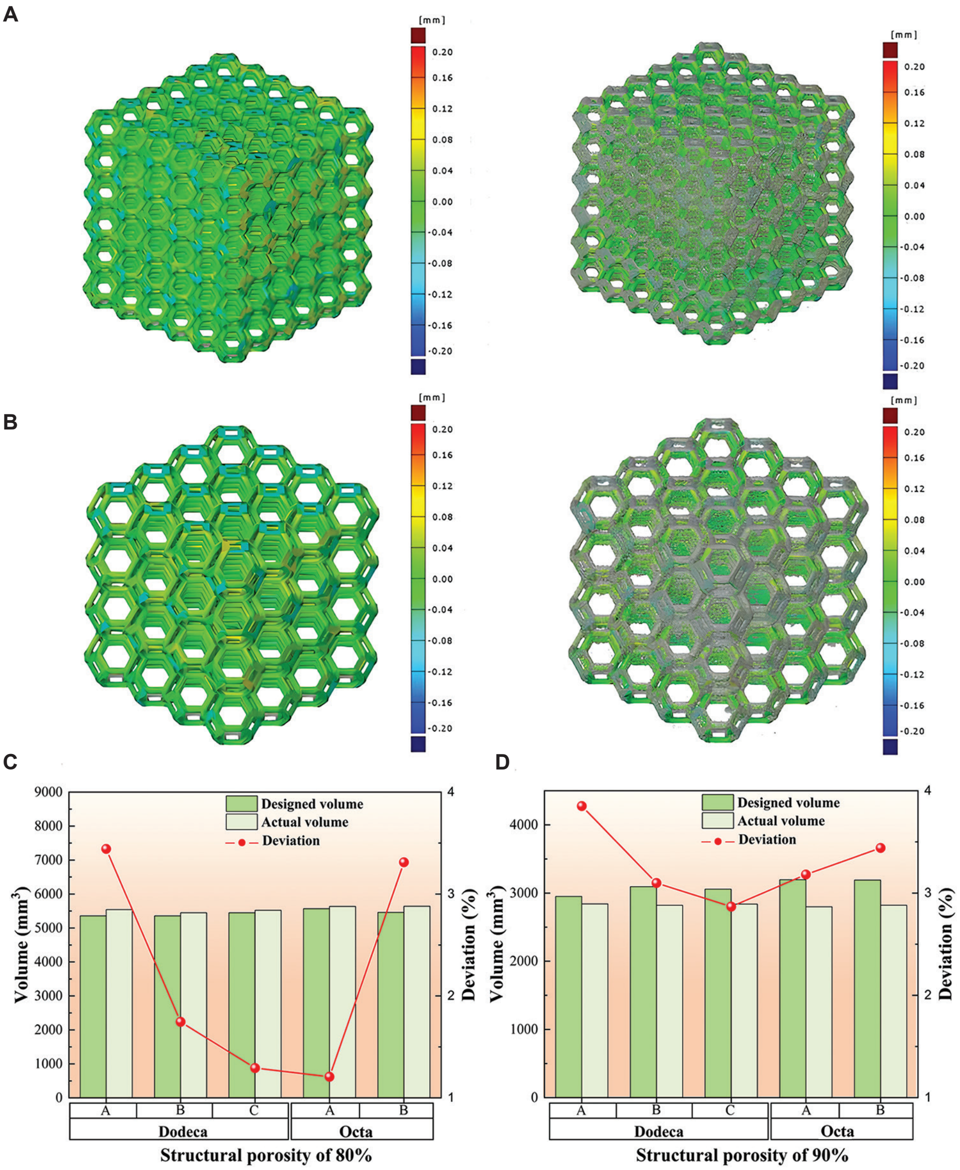

Figure 5. Comparison of the X-ray computed tomography reconstructed models of LPBF-built AlSi10Mg alloy and their corresponding three-dimensional digital models. (A) Octa-A structure with 80% porosity (Octa-A P80), (B) Octa-A structure with 90% porosity (Octa-A P90). Numerical comparison of theoretical and actual volumes of the LPBF-built AlSi10Mg alloy structures, (C) various porous structures with 80% porosity, and (D) various porous structures with 90% porosity

Abbreviations: Octa: Octahedral; LPBF: Laser powder bed fusion

This approach helps reduce the effects of residual stress, facilitates a stable melt pool track, and minimizes defect formation.[42] Due to the intrinsic nature of LPBF, cyclic heating and partial remelting of previous layers result in a distinct melt pool morphology that follows the laser scan tracks. This promotes the formation of large columnar grains extending across multiple melt pool layers along the build direction, introducing significant anisotropy in strength and ductility across various metals.[34,51,52] The morphology and size of single- and multi-track melt pools have been widely studied to understand processing parameters, melt pool stability, and solidification behavior. These studies aim to minimize defects such as porosity, cracking, residual stress, melt pool boundary overlap, and lack of fusion, thereby optimizing the processing window for various aluminum alloys.[42] In addition to achieving high densification and minimal defects, features such as grain size and morphology, orientation, grain boundaries, melt pool borders, and elemental segregation play some roles in determining both static[53-55] and dynamic[4,51] mechanical properties, as well as corrosion performance[31,56,57] for AlSi10Mg and other alloys. Figures 6D and E further show the SEM microstructure of LPBF-fabricated AlSi10Mg samples at low and high magnifications. The SEM images reveal three typical distinct microstructural regions: the melt pool region, the coarse-grain zone, and the heat-affected zone (Figure 6D). The microstructure exhibits a significant presence of network-like cellular structures enriched with silicon (Figure 6E), which is consistent with the findings reported by Liu *et al.*[58] and other literature.[42] Specifically, during LPBF of AlSi10Mg, rapid solidification promotes silicon segregation along the cellular boundaries of the α-Al matrix, forming a silicon-rich eutectic network.[51] Variations in the size and morphology of this network have been shown to significantly influence mechanical performance.[59]

3.2. Dynamic response analysis

Based on the above discussion, the X-CT results reveal that the actual volume and dimensions of the samples fabricated through LPBF closely align with the theoretical design specifications. Furthermore, densification measurements confirm the successful fabrication of LPBF-built AlSi10Mg porous structures with varying unit cell rotations and similar microstructures. The influence of structural porosity errors and material defects induced by the LPBF process on mechanical behavior is not considered in this study, as all samples were produced using identical materials and processing parameters. Accordingly, in this study, consistent LPBF parameters resulted in comparable material density and surface roughness across all structures. Consequently, the discrepancies in mechanical behavior identified in this investigation are primarily attributed to variations in unit cell structure, single-unit cell rotation angles, and porosity level. The subsequent section will examine the dynamic response of these structures, focusing on the effects of varying impact energy levels, porosities, and single-unit cell rotation angles on impact performance.

3.2.1. Effects of varying impact energies on fracture behavior

Distinguishing the effect of varying impact energies on the dynamic mechanical behavior of porous structures is critical for understanding their transient impact resistance and potential applications.[4] In this study, the Dodeca-A structure with 80% porosity (Dodeca-A P80) was first selected for the M1 and M2 impact tests (Table 2) to systematically investigate its mechanical response under varying impact loading conditions. Force-displacement and energy-displacement curves were analyzed to characterize the deformation and energy absorption behavior of the structure, offering key insights into its damage evolution, as shown in Figure 7A and B, respectively. The results indicate that the linear

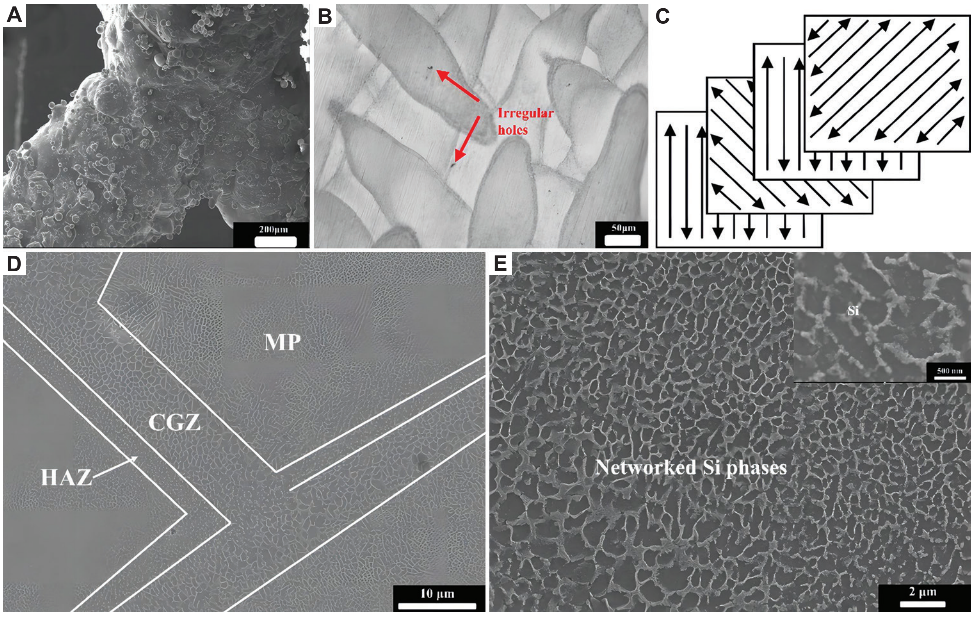

Figure 6. Quality and microstructure of material manufacturing (A) Macroscopic surface of the LPBF-built AlSi10Mg lattice strut regions observed using scanning electron microscopy. Scale bar: 200 μm, magnification: 75×. (B) MP tracks and morphology, exhibiting few irregular pores. (C) Schematic diagram of the scanning strategy used in LPBF. (D) Microstructure of the sample at low magnification. Scale bar: 10 μm, magnification: 2000×. (E) Microstructure of the sample at high magnification, highlighting network-like cellular structures enriched with Si. Scale bars: 500 nm and 2 μm, magnification: 22000×, 9500×

Abbreviations: CGZ: Coarse-grain zone; HAZ: Heat-affected zone; MP: Melt pool; LPBF: Laser powder bed fusion; Si: Silicon stiffness characteristics remain similar across different impact energy levels, suggesting that impact energy has a negligible effect on the linear stiffness of the structure. However, both peak force and energy absorption exhibit significant variations with increasing impact energy. At impact energy of 41 J (M1 in Table 2), the force-displacement curve of the Dodeca-A P80 sample initially exhibits a linear elastic response, followed by a brief oscillation phase before transitioning into a fully compacted state. The small displacement and absence of significant support rod fractures indicate that the applied impact energy is insufficient to cause substantial structural damage, suggesting that the Dodeca-A P80 structure can effectively redistribute stress without failure under low-energy impacts. In contrast, under an impact energy of 124 J (M2 in Table 2), the sample exhibits a prolonged oscillation phase with an extended contact duration before reaching ultimate failure. The structure undergoes noticeable fractures, and the energy-displacement curve gradually increases until the maximum energy absorption capacity is reached. These results highlight the importance of further optimizing the lattice design to enhance the failure resistance of the Dodeca-A P80 structure.

The analysis of fracture modes in the LPBF-fabricated AlSi10Mg porous structures provides critical insights into their mechanical performance under impact loading. During impact, the porous structure undergoes collapse, resulting in the formation of shear fractures with varying inclinations, as illustrated in Figure 8A. Surrounding one edge, obvious cleavage planes are evident throughout the impact fracture (highlighted by the red contour in Figure 8B), primarily observed at the outer edge, where rapid failure occurs due to swift crack propagation. In contrast, the central section of the fracture exhibits a substantial area of dimples, indicative of ductile fracture behavior (Figure 8C). This observation suggests that initial deformation and energy absorption occur at the onset of impact, where crack propagation leads to microvoid

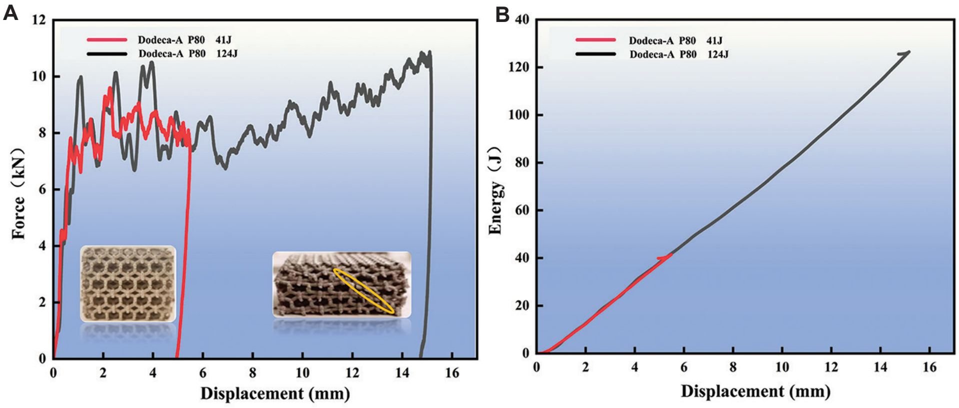

Figure 7. Mechanical response and energy absorption of Dodeca-A structures (A) Force-displacement curves of the laser powder bed fusion-built AlSi10Mg Dodeca-A P80 structure under different impact energies and (B) energy-displacement curves showing energy absorption at varying impact energies
Abbreviation: Dodeca: Dodecahedral

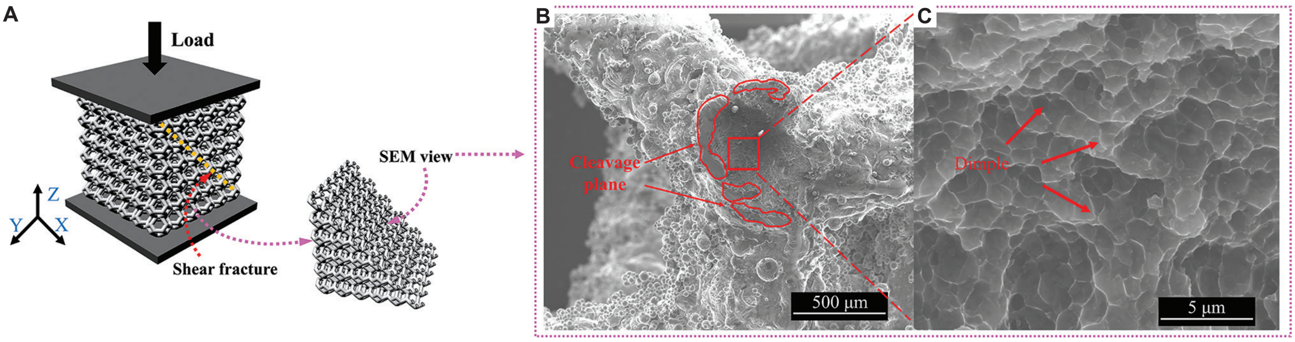

Figure 8. Microscopic morphology of the impact fracture of the dodecahedral-A P80 structure in laser powder bed fusion-fabricated AlSi10Mg. (A) Schematic shear fractures, (B) cleavage planes at the outer edge, and (C) dimpled morphology in the central region (initiation and propagation region). Scale bars: 5 μm and 500 μm, magnification: 18367×, 80×
Abbreviations: SEM: Scanning electron microscopy

formation and dimple rupture before transitioning to rapid brittle cleavage failure. This highlights the typical sequential nature of dynamic fracture processes, such as impact and fatigue deformation.[51] Moreover, the loading distribution and stress concentration in porous structures vary according to the lattice structure design, leading to different deformation modes, as reported in the literature.[2,4,60] These results align with studies in the literature on LPBF-built lattice structures and indicate that fracture characteristics can be further optimized by adjusting strut thickness, unit cell geometry, and porosity levels.[4,8,15]

3.2.2. Influence of unit cell orientation under constant impact energy (124 J)

Impacting structures with different single-unit cell rotation angles at a constant energy level allows an intuitive comparison of performance differences among various designs. When subjected to an impact energy of 124 J, all structures experience oscillatory cycles during the deformation phase (Figure 9). Notably, the intensity of these oscillations is more pronounced in the Dodeca structure (Figure 9A and B) compared to the Octa structure (Figure 9C and D). Within each structure type, those with lower porosity exhibit more intense oscillations than their higher porosity counterparts. This behavior can be attributed to the rapid deformation of high porosity structures under impact loading, which enables a swift transition to a dense state with minimal resistance. Among the Dodeca structures in Figure 9A, variations in oscillation intensity are observed, with Dodeca-A P80 showing the smoothest oscillations, followed by Dodeca-B P80, whereas Dodeca-C P80 displays the most intense oscillations. The intensity of these oscillations reflects changes in the load-carrying capacity of the structures upon impact and indicates the extent of damage sustained. A significant reduction in load-carrying capacity may suggest the occurrence of large fractures within the porous structures. The findings indicate that the geometry and orientation of the single-unit cells influence the oscillation patterns. In addition, as the porosity decreases slightly by 10% (from 90% to 80%) under the same impact energy, the slope of the force-displacement curves increases, indicating a large enhancement in rigidity. There is also a notable variation in the peak force of oscillation among different porosities (Figure 9A-D), highlighting disparities in porous structural strength. The final displacements observed

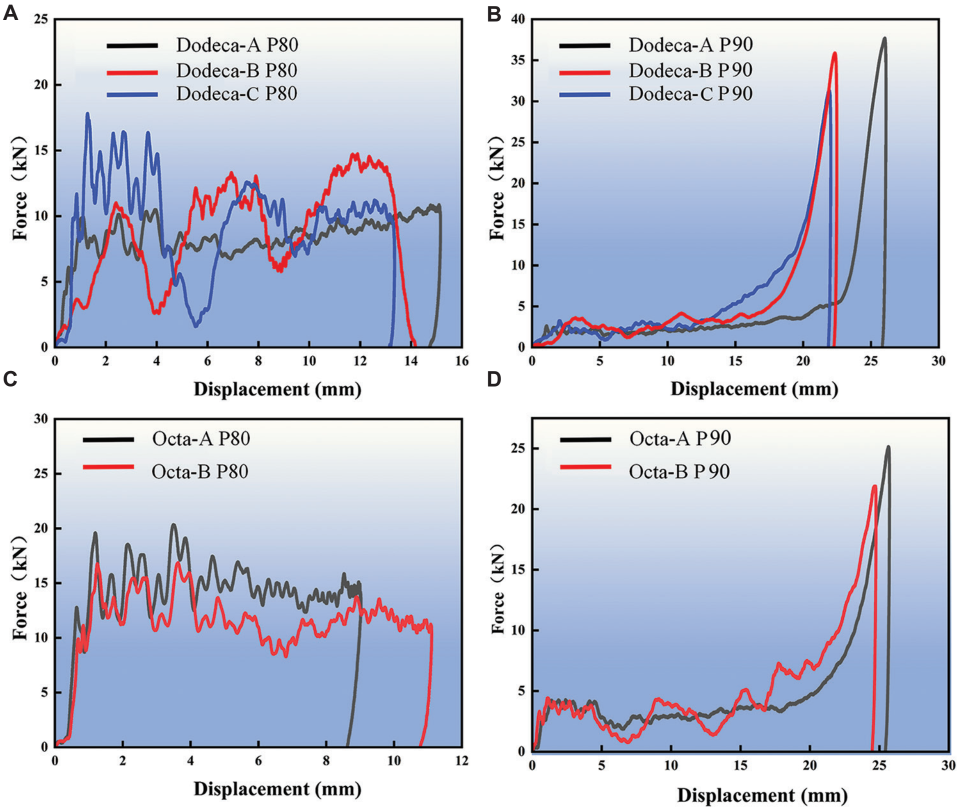

Figure 9. Force-displacement curves under impact loading at an impact energy of 124 J for various porous structures. (A) Dodeca structures with 80% porosity, (B) Dodeca structures with 90% porosity, (C) Octa structures with 80% porosity, and (D) Octa structures with 90% porosity
Abbreviations: Dodeca: Dodecahedral; Octa: Octahedral

indicate the ability of each structure to resist deformation, with Dodeca-C exhibiting the highest resistance among the Dodeca structures at 80% porosity in Figure 9A, followed by Dodeca-B, whereas Dodeca-A demonstrates the lowest resistance. Among the Octa structures in Figure 9C, Octa-A P80 displays superior resistance compared to Octa-B P80. In addition, at this impact energy level, the structure with 90% porosity in Figure 9B and D undergoes rapid deformation and transitions to a dense state, whereas the structure with 80% porosity does not experience this change. This distinction suggests the critical role of optimizing porosity in determining the mechanical response of lightweight structures under impact loading.

Thus, further comparisons of the peak force, energy absorption, and SEA for various structures with 90% porosity are presented in Figure 10. Among the Dodeca structures in Figure 10A, Dodeca-B P90 exhibits the highest peak force at ~3.53 kN, representing a ~33.5% improvement over Dodeca-A P90. Following closely, Dodeca-C P90 achieves a peak force of ~3.26 kN, indicating a ~23.5% enhancement compared to Dodeca-A P90. When evaluating energy absorption, both energy absorption and SEA metrics reveal significant performance differences among the structures. The Dodeca-C P90 structure demonstrates substantial increases in both metrics compared to the Dodeca-A P90, with enhancements of ~18.9% in total energy absorption and ~17.1% in SEA. In contrast, Dodeca-B P90 shows modest improvements, with increases of only ~2.3% and ~1.7%, respectively. Although Dodeca-C P90 does not have the highest peak force, its superior energy absorption profile positions it as the best performer among the Dodeca P90 structures. The notable increase in energy absorption for Dodeca-C indicates that optimizing single-unit cell orientation can effectively enhance the balance between the strength and ductility of the Dodeca structures. For the Octa structures in Figure 10B, Octa-B P90 demonstrates a ~7.22% increase in peak force over Octa-A P90. However, this advantage is offset by a notable reduction in both total energy absorption and SEA, which decline by ~11.7% and ~10.9%, respectively (Figure 10B). Consequently, when considering the performance metrics of the structures, Octa-A P90 is deemed superior despite its lower peak force. The observed performance variations can be attributed to differences in load distribution and deformation mechanisms inherent to each design, which will be investigated later through numerical simulation analysis.

Figure 11 compares the specific strength of Dodeca and Octa structures at 80% porosity, revealing distinct performance trends governed by topology-driven mechanical behavior. Among the Dodeca structures, Dodeca-C P80 exhibits the highest specific strength, significantly surpassing both Dodeca-A P80 and Dodeca-B P80. This enhancement suggests that Dodeca-C's single-unit cell orientation architecture optimizes stress redistribution. In contrast, within the Octa series, Octa-A P80 exhibits a higher specific strength than Octa-B P80, confirming that the single-unit cell orientation does not enhance the performance of Octa-B. Notably, both Octa structures outperform their Dodeca counterparts, indicating that Octa lattice frameworks offer superior strength-to-mass ratios. The observed hierarchy in specific strength aligns closely with the energy absorption characteristics, where Dodeca-C and Octa-A emerge as the most mechanically efficient structures within their respective categories.

3.2.3. Influence of unit cell orientation under high impact energy (248 J)

The sustained energy absorption capacity of porous structures during high-impact events is also vital for applications that require enhanced impact resistance. This section presents the results of high-impact tests conducted on Dodeca P80 and Octa P80 structures exhibiting

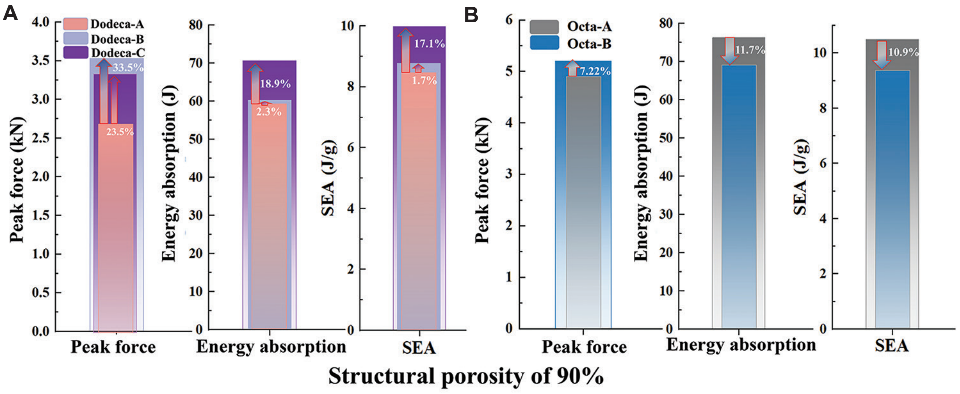

Figure 10. Peak force, energy absorption, and SEA under impact loading at an energy level of 124 J for various LPBF-built AlSi10Mg porous materials with 90% porosity. (A) Dodeca structures and (B) Octa structures

Abbreviations: Dodeca: Dodecahedral; Octa: Octahedral; SEA: Specific energy absorption; LPBF: Laser powder bed fusion

80% porosity, to evaluate how multiple impacts (248 J) influence their energy absorption capabilities. The specific test parameters are summarized in Table 2 under the heading M3. The experimental findings indicate that all porous structure samples achieved complete densification (sudden large spike of the red curve after the yield plateau in Figure 12) after the multiple impacts at a high energy level of 248 J. This behavior highlights a fundamental characteristic of porous materials: Their ability to dissipate energy through deformation and densification under high-energy impacts.[7] For the Dodeca structure, the Dodeca-A P80 underwent a deformation of 6 mm after the multiple impacts before attaining a fully dense state (Figure 12A). In contrast, Dodeca-B and Dodeca-C reached their fully dense states after undergoing 4.3 mm and 8.3 mm deformations, respectively (Figure 12B and C). As illustrated in Figure 13, Dodeca-C P80 demonstrated a remarkable 73.1% increase in energy absorption compared to Dodeca-A P80, showcasing an excellent impact response.

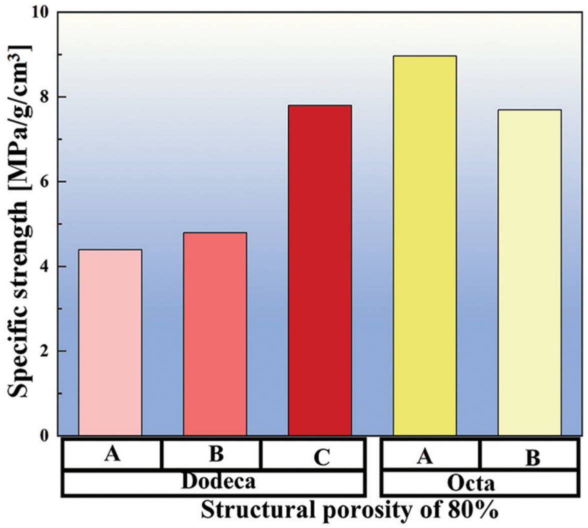

Figure 11. Specific strength of laser powder bed fusion-built AlSi10Mg Dodeca and Octa structures with 80% porosity at different unit cell rotations

Abbreviations: Dodeca: Dodecahedral; Octa: Octahedral

In the case of the Octa structures, the densification process exhibited distinct variations. The Octa-A P80 structure initiated densification at a deformation of 8.6 mm, whereas the Octa-B P80 began this transition at 9.6 mm (Figure 12D and E). Although Octa-A P80 entered the densification phase earlier than Octa-B P80,

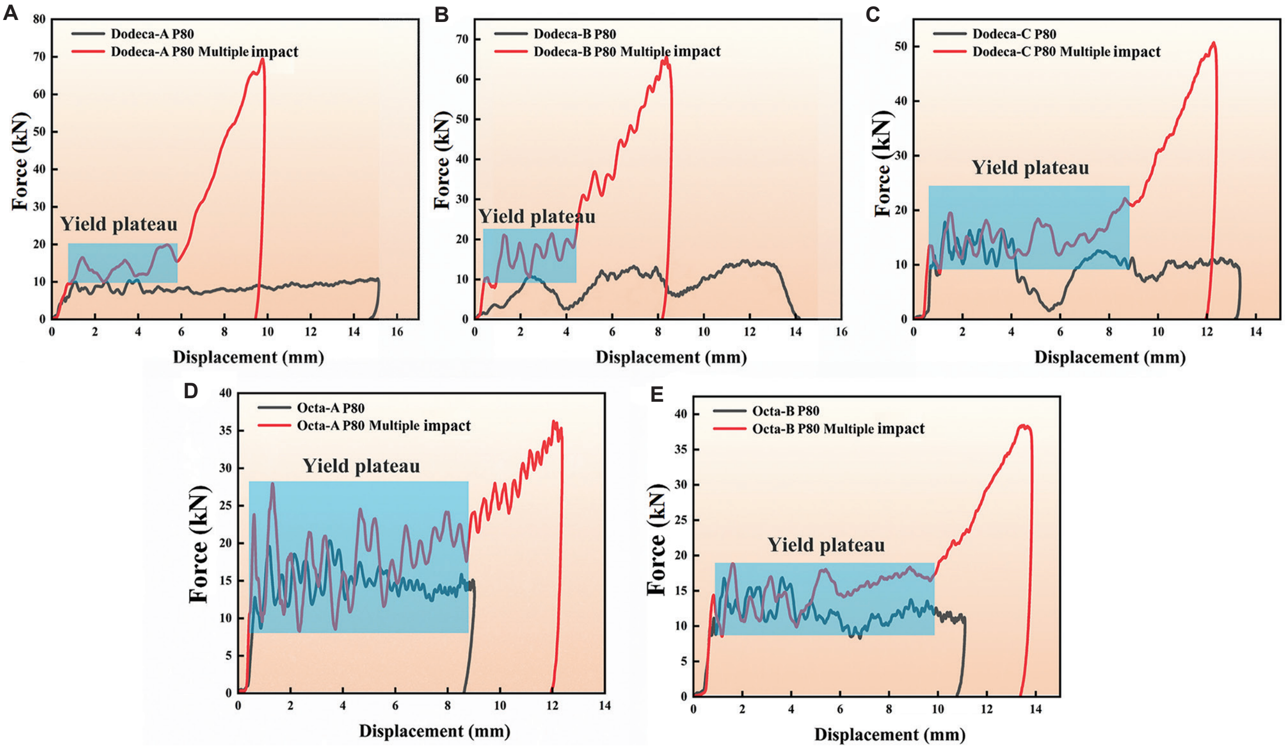

Figure 12. Comparison of force-displacement curves at an impact energy level of 124 J (black curve) and a multiplied energy level of 248 J (red curve) for various laser powder bed fusion-built AlSi10Mg porous structures with 80% porosity. (A) Dodeca-A, (B) Dodeca-B, (C) Dodeca-C, (D) Octa-A, and (E) Octa-B

Abbreviations: Dodeca: Dodecahedral; Octa: Octahedral

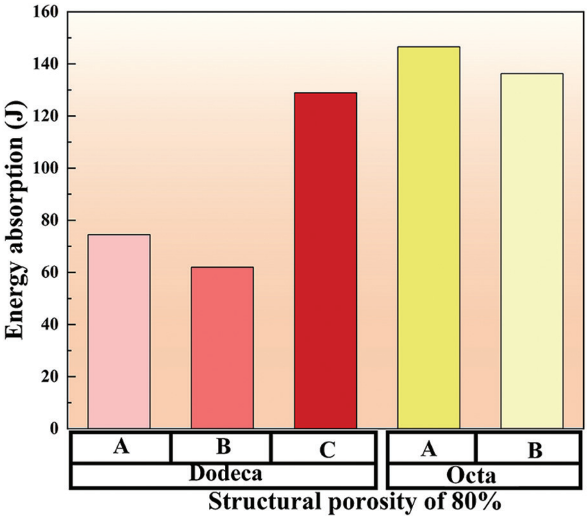

Figure 13. Comparison of energy absorption after two consecutive impacts at a high energy level of 248 J for various porous materials with 80% porosity
Abbreviations: Dodeca: Dodecahedral; Octa: Octahedral

it is noteworthy that Octa-A P80 exhibited a significantly higher yield load, resulting in greater energy absorption capacity. This suggests that the Octa-A structure may possess inherent geometric advantages that promote early load redistribution, contributing to enhanced energy dissipation. In addition, after reaching a deformation of 8.6 mm, Octa-A P80 displayed larger oscillations in load, indicating ongoing resistance within the structure. This behavior contrasts with Octa-B P80, suggesting a rapid loss of structural resistance. Even after transitioning to the post-dense stage, the energy absorption capacity of the Octa-A P80 structure remained superior to that of the Octa-B P80 (Figure 13). These findings highlight the critical role of unit cell orientation in optimizing the energy absorption characteristics of porous structures subjected to higher-impact energies.

3.3. Numerical simulation analysis of impact behavior

The mechanical test results confirm that the orientation angles of single-unit cells significantly influence the impact resistance and energy absorption capabilities of the designed LPBF-built AlSi10Mg Dodeca and Octa porous structures. We further conducted numerical simulations to analyze load-bearing characteristics from a single-unit cell geometrical perspective to deepen our understanding of the different impact behaviors exhibited by various structures with distinct single-unit cell orientations. As shown in Figure 14, the stress-strain behavior of these structures, derived from rotating single-unit cells, was investigated through numerical simulations. Under identical impact loads, single-unit cells with different design structures exhibited varying stress-strain responses (Figure 14). According to Figure 12, under higher impact loads, the structures undergo deformation, leading to eventual failure. Specifically, the simulations demonstrate that different structures and identical single-unit cells with varying rotation angles exhibit distinct capacities for withstanding the same impact load. This confirms that the impact properties of the designed structure are influenced by its rotation angles.

In the Octa series of structures, high-stress concentrations occur at the junctions of the connecting rods (highlighted by red circles in Figure 14) under impact loading. The Octa-A structure, characterized by a greater number of connecting rods and smaller inclination angles, demonstrates enhanced load-bearing capacity compared to the Octa-B structure. When the horizontal connecting rod in Octa-A fails, the components with smaller inclination angles continue to support some load, allowing for partial recovery of structural integrity. In contrast, Octa-B, which is more affected by the horizontal connecting rod at the upper end, transfers the load to the inclined components on both sides. This load transfer leads to fracture and eventual collapse of the entire structure. Consequently, when the strain reaches ~51%, the Octa-A structure retains some load-bearing capacity, whereas Octa-B exhibits greater fracture failure and reduced load-bearing capability.

In the Dodeca series of structures, large stresses are generated at the intersections of the connecting rods at the onset of impact loading (highlighted by red circles in Figure 14), similar to the Octa structures. However, the subsequent deformation manifests distinct stress levels due to differences in unit cell design. Both Dodeca-A and Dodeca-B lack connecting rods with sufficient load-carrying capacity, resulting in suboptimal deformation performance. The absence of adequately angled or positioned connecting rods compromises their ability to redistribute stress effectively, leading to a substantial loss of resistance following the initial fracture. In contrast, the Dodeca-C structure features a greater number of connecting rods with smaller angles relative to the initial direction of the load, enabling it to sustain impact loads more effectively during deformation. Even when some connecting rods fail, the remaining components continue to function (Figure 14, vertical rods in Dodeca-C), providing resistance to impact deformation. Therefore, Dodeca-C exhibits higher impact resistance than the other structures in the Dodeca series, confirming that careful design consideration of rod placement and orientation can yield significant benefits in structural performance. Furthermore, the numerical simulation approach provides a valuable tool for predicting and understanding the performance of porous structures

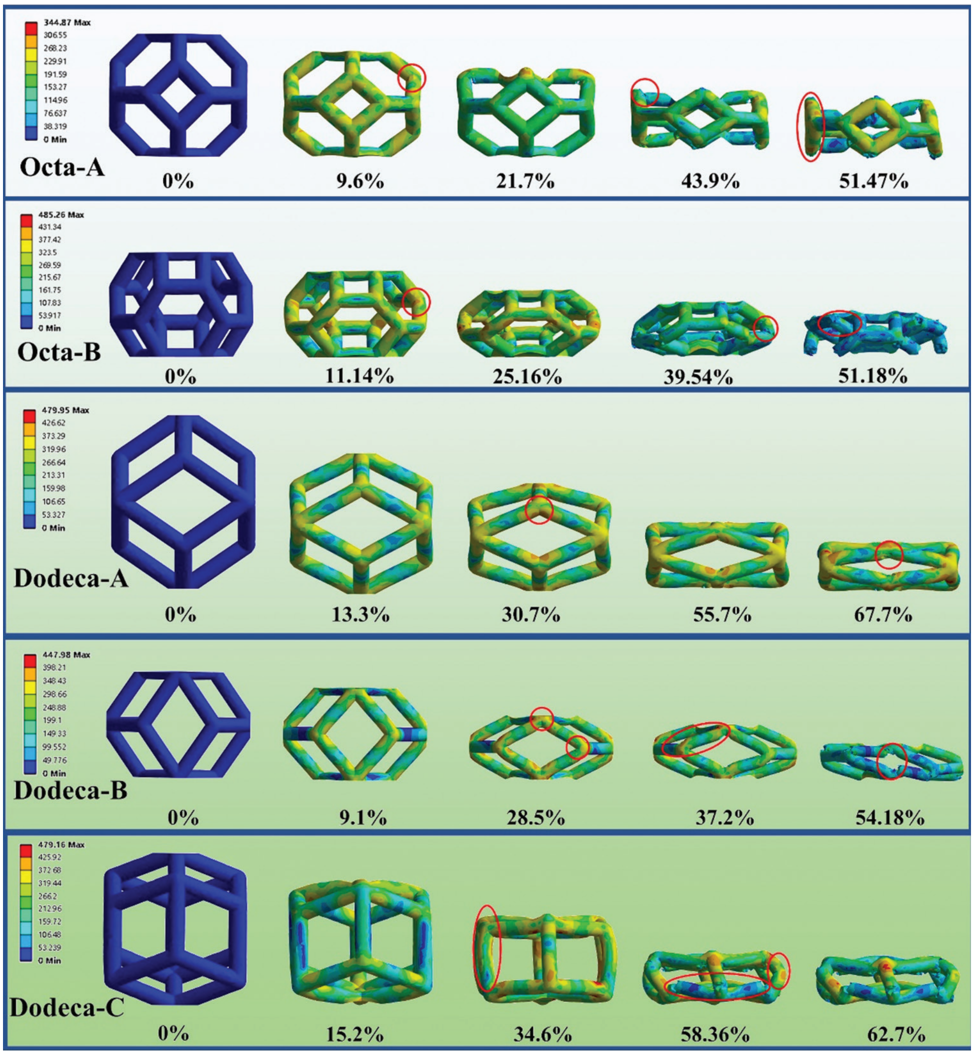

Figure 14. Simulated stress-strain behavior of different structural single-unit cells with rotation under impact loading
Abbreviations: Dodeca: Dodecahedral; Octa: Octahedral

before physical prototyping.[61] The study highlights the potential for optimizing porous structures for enhanced impact resistance from the single-unit cell angle rotation perspective.

The impact resistance of various single-unit cell structures was also assessed by measuring changes in the velocity of an impact hammer (Figure 15). The single-unit cell structures of Dodeca-C and Octa-A were established as reference standards for two major series of structures. The evaluation criterion for the other structures involved identifying the strain at which the Dodeca-C and Octa-A structures reduced the hammer's velocity to 0 mm/s. Throughout the simulation, under uniform strain levels, the falling hammer's velocity exhibited an inverse relationship to the impact resistance of the structures; specifically, higher velocities corresponded to lower impact resistance. Both the Dodeca-A and Dodeca-B structures demonstrated significantly lower impact resistance compared to Dodeca-C, as evidenced by markedly higher hammer fall rates recorded for Dodeca-A and Dodeca-B at a strain of 65.4% (Figure 15). Similarly, Octa-A exhibited superior resistance compared to Octa-B, as shown in the analysis of Figure 15, which aligns with the simulated stress-strain behaviors presented in Figure 14. Overall, the results from the numerical analysis are consistent with the experimental findings, confirming the reliability of the numerical simulations significantly. This agreement suggests that computational modeling can be further utilized to optimize the geometric parameters and predict the mechanical behavior of these design structures for tailored impact properties.

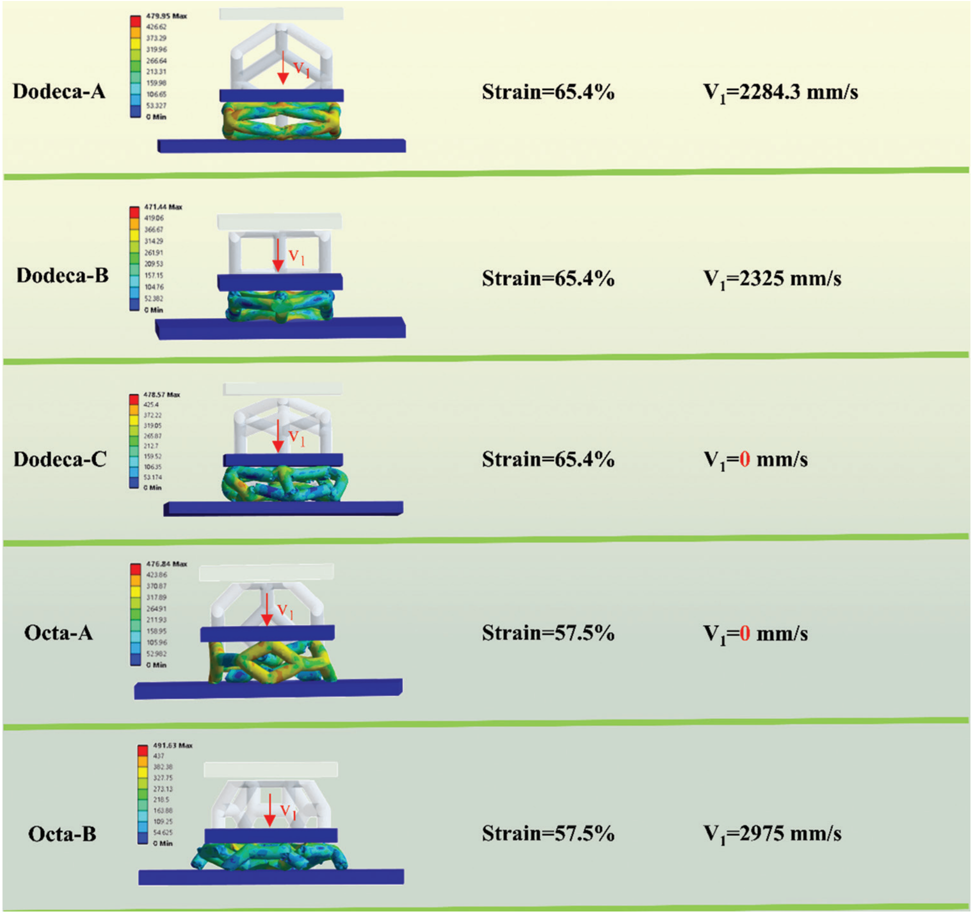

Figure 15. Impact velocity of the falling hammer as a function of strain for different single-unit cell structures
Abbreviations: Dodeca: Dodecahedral; Octa: Octahedral

4. Conclusion

In this study, AlSi10Mg was utilized as the base material, and a series of porous structures were designed using the Voronoi algorithm. These structures were fabricated using LPBF. The dynamic mechanical behavior of the porous structures with 80% and 90% porosity levels was investigated, considering varying single-unit cell rotation angles under different impact energies.

The SEM images reveal a typical LPBF-built AlSi10Mg microstructure with no apparent manufacturing defect pores. The X-CT results indicate that LPBF process parameters have a negligible effect on the dimensional resolution, particularly the porosity consistency, of LPBF-built Dodeca and Octa AlSi10Mg structures with different single-unit cell angle rotations. This consistency ensures that variations in mechanical performance are primarily influenced by structural design rather than inconsistencies in defects or porosity levels.

Porosity level is inversely proportional to energy absorption and impact resistance. Porous structures that experience a slight decrease in porosity of 10% (from 90% to 80%) exhibit significantly higher energy absorption and better impact resistance while maintaining their lightweight features.

The impact resistance of certain structures can be enhanced by rotating single-unit cells, though this approach is not universally applicable. Adjusting the rotation angle improves the impact resistance of Dodeca series structures, such as the Dodeca-C structure, which benefits from a 90° rotation about the Y-axis. In contrast, the rotation negatively affects the impact resistance of the Octa-B structure, leading to decreased performance.

The results demonstrate significant enhancements in energy absorption, SEA, and specific strength, which increase by approximately 18.9% (P90), 17.1% (P90), and 79.5% (P80), respectively, for the rotated single-unit cell Dodeca-C structure compared to the original Dodeca-A counterpart at an impact energy of 124 J. Furthermore, Dodeca-C P80 showed a remarkable 73.1% increase in energy absorption compared to Dodeca-A P80 at a higher impact energy of 248 J.

The experimental results and numerical simulations align, revealing that the Dodeca-C and Octa-A structures exhibit improved energy absorption and impact resistance. This provides a foundation for further single-unit cell rotation design optimization through simulation modeling.

Acknowledgments

J.C. Wang is grateful for the support from the Woodside TechWorks FutrueLab at The University of Western Australia and Woodside Energy Group Ltd.

Funding

The authors are grateful for funding from the Shanghai Sailing Program (Grant number: 19YF1434300), Shanghai Engineering Research Center of High-Performance Medical Device Materials (No. 20DZ2255500), and the National Natural Science Foundation of China (Grant number: 11947137).

Conflicts of interest

The authors declare that they have no known competing financial interests or personal relationships that could have appeared to influence the work reported in this paper.

Author contributions

Conceptualization: Hulin Tang, Songhao Lu, Xuezheng Yue,
Data curation: Songhao Lu, Xuezheng Yue
Formal analysis: Xuezheng Yue, Jincheng Wang
Investigation: Hulin Tang, Shiyue Guo, Rusheng Zhao, Jincheng Wang
Methodology: Hulin Tang, Xuezheng Yue
Software: Hulin Tang
Validation: Hulin Tang, Songhao Lu, Rusheng Zhao, Jincheng Wang
Visualization: Xuezheng Yue
Writing – original draft: Hulin Tang
Writing – review & editing: Boyoung Hur, Xuezheng Yue, Jincheng Wang

Ethics approval and consent to participate

Not applicable.

Consent for publication

Not applicable.

Availability of data

Data are available from the corresponding authors upon reasonable request.

References

1. Babaei M, Kiarasi F, Asemi K, Hosseini M. Functionally graded saturated porous structures: A review. *J Comput Appl Mech*. 2022;53:297-308.

   doi: 10.22059/jcamech.2022.342710.719

2. Wu ZY, Liu YJ, Wu X, Liu XC, Wang JC, Wang Q. Fatigue performance of beta titanium alloy topological porous structures fabricated by laser powder bed fusion. *J Mater Res Technol*. 2024;29:4772-4780.

   doi: 10.1016/j.jmrt.2024.02.190

3. Siddique SH, Hazell PJ, Wang H, Escobedo JP, Ameri AAH. Lessons from nature: 3D printed bio-inspired porous structures for impact energy absorption-A review. *Addit Manuf*. 2022;58:103051.

   doi: 10.1016/j.addma.2022.103051

4. Wu ZY, Liu YJ, Bai HW, *et al.* Microstructure and mechanical behavior of rhombic dodecahedron-structured porous β-Ti composites fabricated via laser powder bed fusion. *J Mater Res Technol*. 2024;31:298-310.

   doi: 10.1016/j.jmrt.2024.06.077

5. Wang B, Luo M, Shi Z, *et al.* Porous titanium alloys for medical application: Progress in preparation process and surface modification research. *MSAM*. 2024;3:2753.

   doi: 10.36922/msam.2753

6. Dul'nev GN, Volkov DP, Malarev VI. Thermal conductivity of moist porous materials. *J Eng Phys*. 1989;56:198-206.

   doi: 10.1007/BF00870578

7. Yin H, Zhang W, Zhu L, Meng F, Liu J, Wen G. Review on lattice structures for energy absorption properties. *Compos Struct*. 2023;304:116397.

   doi: 10.1016/j.compstruct.2022.116397

8. Xu K, Cao J, Zheng Z, *et al.* Deformation behavior of inconel 625 alloy with TPMS structure. *Materials* (*Basel*). 2025;18:396.

   doi: 10.3390/ma18020396

9. Lu S, Zhang M, Guo S, Hur B, Yue X. Numerical investigation of impact behavior of strut-based cellular structures designed by spatial voronoi tessellation. *Metals*. 2022;12:1189.

   doi: 10.3390/met12071189

10. Ha NS, Pham TM, Hao H, Lu G. Energy absorption characteristics of bio-inspired hierarchical multi-cell square tubes under axial crushing. *Int J Mech Sci*. 2021;201:106464.

    doi: 10.1016/j.ijmecsci.2021.106464

11. Ha NS, Pham TM, Tran TT, Hao H, Lu G. Mechanical properties and energy absorption of bio-inspired hierarchical circular honeycomb. *Compos Part B Eng*. 2022;236:109818.

    doi: 10.1016/j.compositesb.2022.109818

12. Zhang L, Feih S, Daynes S, *et al.* Energy absorption characteristics of metallic triply periodic minimal surface sheet structures under compressive loading. *Addit Manuf*. 2018;23:505-515.

    doi: 10.1016/j.addma.2018.08.007

13. Zhao M, Zhang DZ, Liu F, Li Z, Ma Z, Ren Z. Mechanical and energy absorption characteristics of additively manufactured functionally graded sheet lattice structures with minimal surfaces. *Int J Mech Sci*. 2020;167:105262.

    doi: 10.1016/j.ijmecsci.2019.105262

14. Hu D, Mei X, Shi P, Zhou X. Inner-pipe structure to improve column heterogeneity and peak shape. *J Chromatogr Sci*. 2014;53:565-570.

    doi: 10.1093/chromsci/bmu085

15. Liu YJ, Zhang ZL, Wang JC, *et al. In-situ* micro-CT analysis of deformation behavior in sandwich-structured metastable beta Ti-35Nb alloy. *Trans Nonferrous Met Soc China*. 2024;34:2552-2562.

    doi: 10.1016/S1003-6326(24)66559-3

16. Wang Z. Recent advances in novel metallic honeycomb structure. *Compos Part B Eng*. 2019;166:731-741.

    doi: 10.1016/j.compositesb.2019.02.011

17. Song ZL, Ma LQ, Wu ZJ, He DP. Effects of viscosity on cellular structure of foamed aluminum in foaming process. *J Mater Sci*. 2000;35:15-20.

    doi: 10.1023/A:1004715926692

18. Zhang M, Bi G, Chen J. Research on impact resistance of AlSi7Mg uniform and gradient porous structures manufactured by laser powder bed fusion. *MSAM*. 2024;3:5729.

    doi: 10.36922/msam.5729

19. Al-Saedi DSJ, Masood SH, Faizan-Ur-Rab M, Alomarah A, Ponnusamy P. Mechanical properties and energy absorption capability of functionally graded F2BCC lattice fabricated by SLM. *Mater Des*. 2018;144:32-44.

    doi: 10.1016/j.matdes.2018.01.059

20. Liu YJ, Zhang JS, Liu XC, *et al.* Non-layer-wise fracture and deformation mechanism in beta titanium cubic lattice structure manufactured by selective laser melting. *Mater Sci Eng A*. 2021;822:141696.

    doi: 10.1016/j.msea.2021.141696

21. Şerban DA, Negru R, Sărăndan S, Belgiu G, Marşavina L. Numerical and experimental investigations on the mechanical properties of cellular structures with open Kelvin cells. *Mech Adv Mater Struct*. 2021;28:1367-1376.

    doi: 10.1080/15376494.2019.1669093

22. Lovinger Z, Czarnota C, Ravindran S, Molinari A, Ravichandran G. The role of micro-inertia on the shock structure in porous metals. *J Mech Phys Solids*. 2021;154:104508.

    doi: 10.1016/j.jmps.2021.104508

23. Czarnota C, Molinari A, Mercier S. Steady shock waves in porous metals: Viscosity and micro-inertia effects. *Int J Plast*. 2020;135:102816.

    doi: 10.1016/j.ijplas.2020.102816

24. Fíla T, Koudelka P, Falta J, *et al.* Dynamic impact testing of cellular solids and lattice structures: Application of two-sided direct impact Hopkinson bar. *Int J Impact Eng*. 2021;148:103767.

    doi: 10.1016/j.ijimpeng.2020.103767

25. Jin N, Wang F, Wang Y, Zhang B, Cheng H, Zhang H. Failure and energy absorption characteristics of four lattice structures under dynamic loading. *Mater Des*. 2019;169:107655.

    doi: 10.1016/j.matdes.2019.107655

26. Cao X, Duan S, Liang J, Wen W, Fang D. Mechanical properties of an improved 3D-printed rhombic dodecahedron stainless steel lattice structure of variable cross section. *Int J Mech Sci*. 2018;145:53-63.

    doi: 10.1016/j.ijmecsci.2018.07.006

27. Kim JH, Kim D, Lee MG, Lee JK. Multiscale analysis of open-cell aluminum foam for impact energy absorption. *J Mater Eng Perform*. 2016;25:3977-3984.

    doi: 10.1007/s11665-016-2187-0

28. Tancogne-Dejean T, Spierings AB, Mohr D. Additively-manufactured metallic micro-lattice materials for high specific energy absorption under static and dynamic loading. *Acta Mater*. 2016;116:14-28.

    doi: 10.1016/j.actamat.2016.05.054

29. Wang JC, Liu YJ, Rabadia CD, Liang SX, Sercombe TB, Zhang LC. Microstructural homogeneity and mechanical behavior of a selective laser melted Ti-35Nb alloy produced from an elemental powder mixture. *J Mater Sci Technol*. 2021;61:221-233.

    doi: 10.1016/j.jmst.2020.05.052

30. Zheng Z, Qiu S, Yue X, Wang J, Hou J. Detecting irradiation defects in materials: A machine learning approach to analyze helium bubble images. *J Nucl Mater*. 2024;596:155117.

    doi: 10.1016/j.jnucmat.2024.155117

31. Lu WQ, Liu YJ, Wu X, Liu XC, Wang JC. Corrosion and passivation behavior of Ti-6Al-4V surfaces treated with high-energy pulsed laser: A comparative study of cast and 3D-printed specimens in a NaCl solution. *Surf Coat Technol*. 2023;470:129849.

    doi: 10.1016/j.surfcoat.2023.129849

32. Wei SY, Ji LN, Wu WJ, Ma HL. Selective laser melting

of lanthanum oxide-reinforced tungsten composites: Microstructure and mechanical properties. *Tungsten*. 2022;4:67-78.

doi: 10.1007/s42864-021-00127-0

33. Ma HY, Wang JC, Qin P, *et al.* Advances in additively manufactured titanium alloys by powder bed fusion and directed energy deposition: Microstructure, defects, and mechanical behavior. *J Mater Sci Technol*. 2024;183:32-62.

    doi: 10.1016/j.jmst.2023.11.003

34. Ma HY, Wang JC, Liu YJ, *et al. In-situ* microstructural evolution and deformation mechanisms of metastable beta titanium fabricated by laser powder bed fusion under flexural stress. *Mater Sci Eng A*. 2025;925:147873.

    doi: 10.1016/j.msea.2025.147873

35. Wang JC, Liu YJ, Liang SX, *et al.* Comparison of microstructure and mechanical behavior of Ti-35Nb manufactured by laser powder bed fusion from elemental powder mixture and prealloyed powder. *J Mater Sci Technol*. 2022;105:1-16.

    doi: 10.1016/j.jmst.2021.07.021

36. Zhang LC, Wang JC. Stabilizing 3D-printed metal alloys. *Science*. 2024;383:586-587.

    doi: 10.1126/science.adn6566

37. Lu W, Liu Y, Wu X, Liu X, Wang J. Corrosion behavior and microstructural effects on passivation film mechanisms in forged Ti-5Al-5Mo-5V-1Cr-1Fe titanium alloy under laser surface remelting. *Corros Sci*. 2024;241:112542.

    doi: 10.1016/j.corsci.2024.112542

38. Wang JC, Liu YJ, Qin P, Liang SX, Sercombe TB, Zhang LC. Selective laser melting of Ti–35Nb composite from elemental powder mixture: Microstructure, mechanical behavior and corrosion behavior. *Mater Sci Eng A*. 2019;760:214-224.

    doi: 10.1016/j.msea.2019.06.001

39. Nie X, Chen Z, Qi Y, Zhang H, Zhu H. Spreading behavior and hot cracking mechanism of single tracks in high strength Al–Cu–Mg–Mn Alloy fabricated by laser powder bed fusion. *Acta Metall Sin* (*Engl Lett*). 2023;36:1454-1464.

    doi: 10.1007/s40195-023-01553-4

40. Lin S, Deng YL, Lin HQ, *et al.* Microstructure, mechanical properties and stress corrosion behavior of friction stir welded joint of Al–Mg–Si alloy extrusion. *Rare Met*. 2023;42:2057-2067.

    doi: 10.1007/s12598-018-1126-7

41. Sun SB, Zheng LJ, Liu JH, Zhang H. Microstructure, cracking behavior and control of Al–Fe–V–Si alloy produced by selective laser melting. *Rare Met*. 2023;42:1353-1362.

    doi: 10.1007/s12598-016-0846-9

42. Wang JC, Zhu R, Liu YJ, Zhang LC. Understanding melt pool characteristics in laser powder bed fusion: An overview of single and multi-track melt pools for process optimization. *Adv Powder Mater*. 2023;2:100137.

    doi: 10.1016/j.apmate.2023.100137

43. Guo S, Yue X, Kitazono K. Anisotropic compression behavior of additively manufactured porous titanium with ordered open-cell structures at different temperatures. *Mater Trans*. 2021;62:1771-1776.

    doi: 10.2320/matertrans.MT-M2021149

44. Bezci SE, Klineberg EO, O'Connell GD. Effects of axial compression and rotation angle on torsional mechanical properties of bovine caudal discs. *J Mech Behav Biomed Mater*. 2018;77:353-359.

    doi: 10.1016/j.jmbbm.2017.09.022

45. Yang J, Gu D, Lin K, *et al.* Laser powder bed fusion of mechanically efficient helicoidal structure inspired by mantis shrimp. *Int J Mech Sci*. 2022;231:107573.

    doi: 10.1016/j.ijmecsci.2022.107573

46. Aktürk M, Boy M, Gupta MK, Waqar S, Krolczyk GM, Korkmaz ME. Numerical and experimental investigations of built orientation dependent Johnson-Cook model for selective laser melting manufactured AlSi10Mg. *J Mater Res Technol*. 2021;15:6244-6259.

    doi: 10.1016/j.jmrt.2021.11.062

47. Nurel B, Nahmany M, Frage N, Stern A, Sadot O. Split Hopkinson pressure bar tests for investigating dynamic properties of additively manufactured AlSi10Mg alloy by selective laser melting. *Addit Manuf*. 2018;22:823-833.

    doi: 10.1016/j.addma.2018.06.001

48. Hou Y, Li Y, Cai X, *et al.* Mechanical response and response mechanism of AlSi10Mg porous structures manufactured by laser powder bed fusion: Experimental, theoretical and numerical studies. *Mater Sci Eng A*. 2022;849:143381.

    doi: 10.1016/j.msea.2022.143381

49. Andrew JJ, Schneider J, Ubaid J, Velmurugan R, Gupta NK, Kumar S. Energy absorption characteristics of additively manufactured plate-lattices under low- velocity impact loading. *Int J Impact Eng*. 2021;149:103768.

    doi: 10.1016/j.ijimpeng.2020.103768

50. Al-Ketan O, Rowshan R, Abu Al-Rub RK. Topology-mechanical property relationship of 3D printed strut, skeletal, and sheet based periodic metallic cellular materials. *Addit Manuf*. 2018;19:167-183.

    doi: 10.1016/j.addma.2017.12.006

51. Paul MJ, Liu Q, Best JP, *et al.* Fracture resistance of AlSi10Mg fabricated by laser powder bed fusion. *Acta Mater*. 2021;211:116869.

    doi: 10.1016/j.actamat.2021.116869

52. Peters M, Brodie EG, Thomas S, *et al.* On the importance of nano-oxide control in laser powder bed fusion manufactured Ni-based alloys to enhance fracture properties. *Materialia*. 2023;32:101958.

    doi: 10.1016/j.mtla.2023.101958

53. Shenghao C, Xiang W, Haowei B, Yujing L, Yihao W, Jincheng W. Effects of selective laser surface treatment on plasticity of 2060 Al-Li alloy. *Spec Cast Nonferrous Alloys*. 2025;45:334-341.

    doi: 10.15980/j.tzzz.T20240066

54. Wang R, Wang J, Lei LM, *et al.* Laser additive manufacturing of strong and ductile Al-12Si alloy under static magnetic field. *J Mater Sci Technol*. 2023;163:101-112.

    doi: 10.1016/j.jmst.2023.04.021

55. Sheng X, Guo A, Guo S, *et al.* Laser powder bed fusion for the fabrication of triply periodic minimal surface lattice structures: Synergistic macroscopic and microscopic optimization. *J Manuf Process*. 2024;119:179-192.

    doi: 10.1016/j.jmapro.2024.03.081

56. Chen R, Zheng C, Ma H, *et al.* Multi-parameter optimization and corrosion behavior of FeCoNiCrAl HEA coatings via laser cladding. *Metals*. 2025;15:406.

    doi: 10.3390/met15040406

57. Rubben T, Revilla RI, De Graeve I. Influence of heat treatments on the corrosion mechanism of additive manufactured AlSi10Mg. *Corros Sci*. 2019;147:406-415.

    doi: 10.1016/j.corsci.2018.11.038

58. Liu B, Li BQ, Li Z. Selective laser remelting of an additive layer manufacturing process on AlSi10Mg. *Results Phys*. 2019;12:982-988.

    doi: 10.1016/j.rinp.2018.12.018

59. Li Z, Li Z, Tan Z, Xiong DB, Guo Q. Stress relaxation and the cellular structure-dependence of plastic deformation in additively manufactured AlSi10Mg alloys. *Int J Plast*. 2020;127:102640.

    doi: 10.1016/j.ijplas.2019.12.003

60. Wang H, Fu Y, Su M, Hao H. Effect of structure design on compressive properties and energy absorption behavior of ordered porous aluminum prepared by rapid casting. *Mater Des*. 2019;167:107631.

    doi: 10.1016/j.matdes.2019.107631

61. Chua C, Sing SL, Chua CK. Characterisation of *in-situ* alloyed titanium-tantalum lattice structures by laser powder bed fusion using finite element analysis. *Virtual Phys Prototyp.* 2023;18:e2138463.

    doi: 10.1080/17452759.2022.2138463